

Chapter 1

Phase-conjugate optical coherence tomography

The past two decades have witnessed a number of experiments focused on the use of quantum-entangled states of light to achieve interesting effects. For example, quantum optical coherence tomography (Q-OCT) proposed by Abouraddy et al. [1] and later demonstrated by Nasr et al. [20], utilized maximally entangled photon states and Hong-Ou-Mandel interferometry [15] to achieve a $2\times$ axial resolution improvement and dispersion cancellation over standard conventional OCT.

Such effects, including the resolution afforded by the width of the Hong-Ou-Mandel interference, and dispersion cancellation [22, 12], were initially thought to be distinctly non-classical. However, much early research overlooked the possibility of classical light sources that have no entanglement but are merely maximally correlated in the classical, stochastic sense. Recent advances in nonlinear optical crystals and a better understanding of parametric downconversion have permitted us to generate a variety of these interesting classical light fields that bear properties previously associated exclusively with quantum optics. Of particular note is the ability to generate classical biphoton states that are coincident in time with classically-maximal phase-sensitive correlations.

In particular, in the case of Q-OCT, Erkmen and Shapiro [9] have shown that both the $2\times$

axial resolution improvement and dispersion cancellation are not exclusively quantum effects, but merely a result of the phase-sensitive cross-correlation between the signal and idler biphoton state. This leads to the question of whether the same advantages can be obtained from an experiment with classical phase-sensitive light sources, which are uncommon but can be experimentally constructed. Erkmen and Shapiro proposed such a technique [9], called phase-conjugate optical coherence tomography (PC-OCT) which uses an unconventional arrangement using only classical light sources and classical photodetectors to achieve both of these advantages previously associated with Q-OCT.

In this chapter we explore classical, quantum, and phase-conjugate OCT configurations, build a parametric downconversion-based source to implement classical phase-sensitive light, use it to implement PC-OCT.

1.1 Optical coherence tomography configurations

Optical coherence tomography (OCT) is a three-dimensional imaging technique that employs interference measurements to derive axial resolution. We explore three main techniques by which this is accomplished: conventional OCT (C-OCT), quantum OCT (Q-OCT), and phase-conjugate OCT (PC-OCT). In our analysis we disregard transverse scanning, and focus solely on axial (depth) resolution which is the differentiating aspect of the three methods.

1.1.1 Conventional OCT

The basic principle of C-OCT is shown in figure 1-1. C-OCT uses classical signal and reference light beams that have phase-insensitive cross-correlations, as might be generated using any classical high-flux source with a short coherence length (such as an LED or pulsed laser source) and a 50/50 beamsplitter. The signal beam interrogates the sample and the reflected light is recombined with the reference beam using a simple Michelson interferometer to measure the second-order correlations between the two beams. As the path length of either beam is scanned, the interference envelope reflects the axial profile of the target.

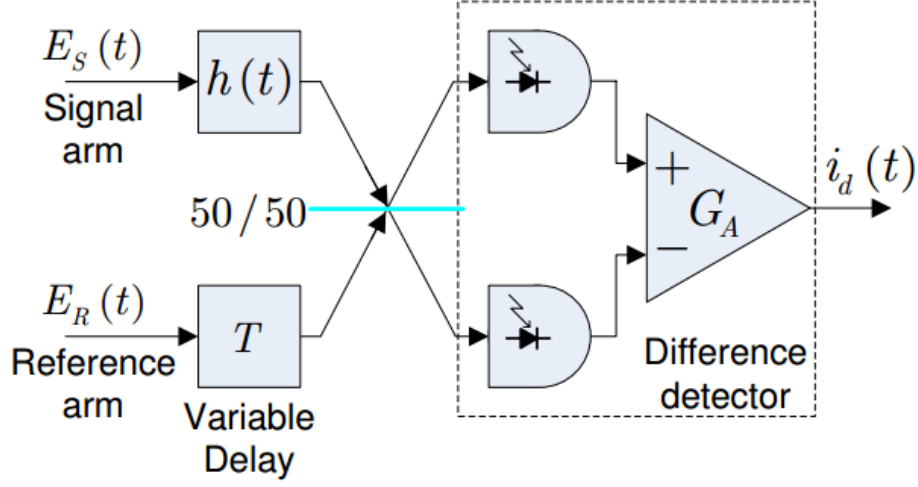


Figure 1-1: Schematic of conventional optical coherence tomography (C-OCT).

Erkmen describes in [8] the analytic computation of the interference signature of C-OCT, which we briefly summarize here. We assume classical zero-mean, stationary, jointly Gaussian signal and reference fields with complex envelopes $E_S(t)$ and $E_R(t)$ with powers $\hbar\omega_0|E_K(t)|^2$ for $K = S, R$, respectively. In the case of C-OCT there are no phase-sensitive cross-correlations, and these fields are completely characterized by their phase-insensitive auto- and cross-correlations:

$$\langle E_J^*(t + \tau) E_K(t) \rangle = F^{-1}[S(\Omega)] \quad (1.1)$$

for $J, K = S, R$ where

$$F^{-1}[S(\Omega)] = \int_{-\infty}^{\infty} \frac{d\Omega}{2\pi} S(\Omega) e^{i\Omega\tau} \quad (1.2)$$

is the inverse Fourier transform of $S(\Omega)$ and $S(\Omega) = S(-\Omega)$ is the common spectrum of

the signal and reference beams at $\pm\Omega$ from the center frequency ω_0 . We assume a target with an axial profile $h(t)$ and baseband impulse response $H(\Omega) = F[h(t)]$. In the case of a weakly reflecting mirror located at time delay T_0 and complex reflectivity r with $|r| \ll 1$, this baseband impulse response is defined by:

$$H(\Omega) = r e^{i(\omega_0 + \Omega)T_0} \quad (1.3)$$

After the signal field $E_S(t)$ interacts with the sample, the resulting field is described by the convolution of $E_S(t)$ with $h(t)$. An interferometric measurement is then made with the reference beam $E_R(t)$ delayed by time T . As shown by Erkmen and Shapiro [9], the resulting interferometric envelope is given by

$$\langle i_d(t) \rangle = 2q\eta G_A R e \left(\int_{-\infty}^{\infty} \frac{d\Omega}{2\pi} H^*(-\Omega) S(\Omega) e^{-i(\Omega - \omega_0)T} \right) \quad (1.4)$$

Note that this envelope is linear in $H(\Omega)$. If we insert the response of the weakly reflecting mirror, we obtain an envelope proportional to $e^{\Omega_S^2(T_0 - T)^2/2}$. For a source with bandwidth Ω_S , this gives us an axial resolution of $4/\Omega_S$, where we define resolution as the full-width between the e^{-2} attenuation points of the visibility envelope.

Note also that C-OCT is vulnerable to dispersion in the sample, which will manifest itself inside $H(\Omega)$. Due to the linear dependence on $H(\Omega)$, there will be no dispersion-cancelling properties in C-OCT.

1.1.2 Quantum OCT

In Q-OCT, first proposed by Abouraddy et al. [1], the signal and reference beams are replaced by an entangled biphoton source and the Michaelson interferometer is replaced by a Hong-Ou-Mandel interferometric measurement, as shown in figure 1-2. In order to analyze Q-OCT we must use quantum fields. Suppose we have signal and reference beams with photon-unit field operators $\hat{E}_S(t)$ and $\hat{E}_R(t)$, respectively, with commutators

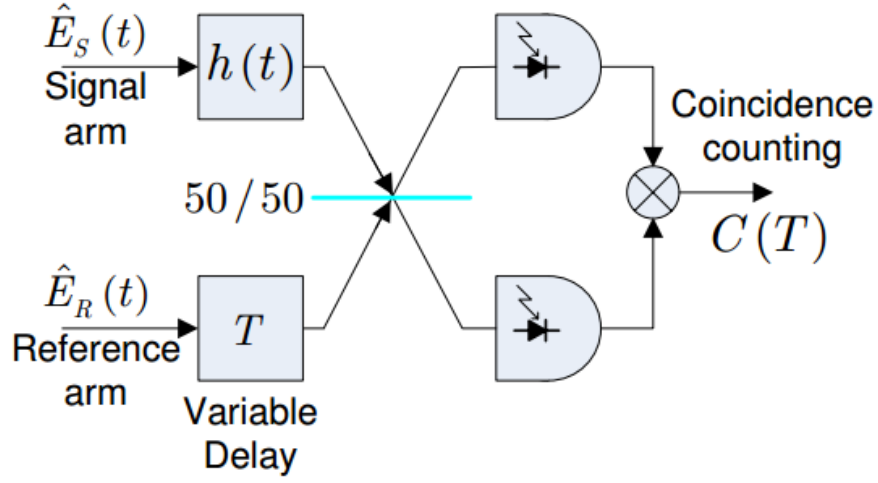


Figure 1-2: Schematic of Quantum optical coherence tomography (Q-OCT).

$$[\hat{E}_J(t), \hat{E}_K^+(u)] = \delta_{JK} \delta(t - u) \quad (1.5)$$

for $J, K = S, R$. We further assume that the fields have the maximum phase-sensitive cross-correlation permitted by quantum mechanics:

$$\langle \hat{E}_S(t + \tau) \hat{E}_R(t) \rangle = F^{-1}[\sqrt{S(\Omega)(S(\Omega) + 1)}] \quad (1.6)$$

Under these conditions, and in the biphoton limit where HOM is usually performed, $S(\Omega)$ and the photon coincidence counting signature is shown by Erkmen and Shapiro [9] to be:

$$\langle C(T) \rangle = \frac{q^2 \eta^2}{2} \left[\int_{-\infty}^{\infty} \frac{d\Omega}{2\pi} |H(\Omega)|^2 S(\Omega) - \text{Re} \left(\int_{-\infty}^{\infty} \frac{d\Omega}{2\pi} H^*(-\Omega) H(\Omega) S(\Omega) e^{-i2\Omega T} \right) \right] \quad (1.7)$$

Using the same partially-reflecting mirror, the dip in the coincidence counts is proportional to $e^{-2\Omega_S^2(T_0-T)^2}$. Note that by the same resolution definition, we obtain an axial resolution of $2/\Omega_S$ which is twice the resolution as C-OCT for the same source bandwidth Ω_S . Moreover, note that unlike C-OCT, the HOM dip term of 1.7 is nonlinear in $H(\Omega)$ and involves a phase conjugation which will result in the cancellation of all even-order dispersion in the sample.

1.1.3 Phase-conjugate OCT

Although these advantages were earlier attributed to quantum effects, Erkmen and Shapiro showed that they are merely results of the phase-sensitive coherence between the signal and idler and achievable using PC-OCT [9], whose block diagram is shown in figure 1-3. In this configuration, the signal and idler are classical sources with phase-sensitive cross-correlations. The sample is interrogated twice at the same point with phase conjugation between the two passes.

In PC-OCT, we assume classical signal and idler fields $E_S(t)$ and $E_R(t)$ with maximal phase-sensitive correlations as permitted by classical physics. The signal beam $E_S(t)$ is focused on a target with axial profile $h(t) = F^{-1}[H(\Omega)]$. The resulting field is

$$E_H(t) = E_S(t) * h(t) \quad (1.8)$$

where $*$ denotes convolution. We then pass $E_H(t)$ into a conjugate amplifier with impulse response $v(t)$, resulting in the field:

$$E_C(t) = (E_H^*(t) + w(t)) * v(t) \quad (1.9)$$

where $w(t)$ is zero-mean white Gaussian quantum noise injected by the conjugation process, satisfying ..., and $v(t)$ is the impulse response of the conjugator. After conjugation, the light is focused onto the same sample a second time, resulting in the field

$$E_1(t) = (E_C(t) * h(t)) * e^{-i\omega_0 t} \quad (1.10)$$

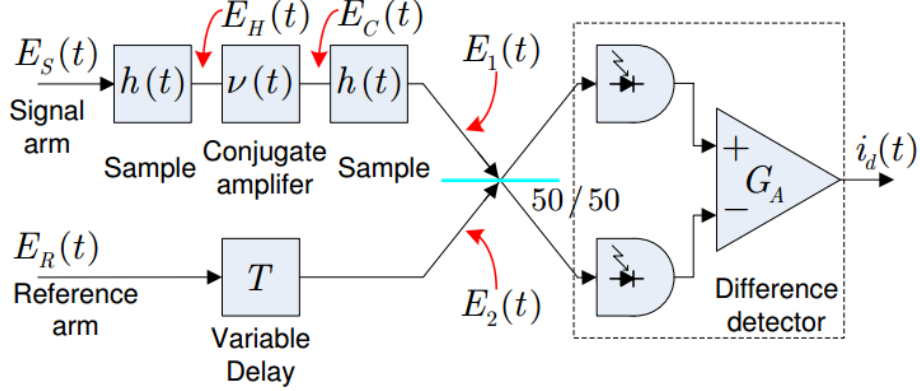


Figure 1-3: Schematic of Phase-conjugate optical coherence tomography (PC-OCT).

We then recombine $E_1(t)$ with the reference beam, delayed by T , in a Michaelson interferometer, yielding an interference signature of

$$\langle i_d(t) \rangle = 2q\eta G_A \text{Re} \left(\int_{-\infty}^{\infty} \frac{d\Omega}{2\pi} H^*(-\Omega) H(\Omega) V^*(-\Omega) S(\Omega) e^{-i(\Omega - \omega_0)T} \right) \quad (1.11)$$

This interference signature bears much resemblance to the second term of the interference signature of Q-OCT; both PC-OCT and Q-OCT have $H^*(\Omega)H(-\Omega)$ dependence. Indeed, if we use the same $H(\Omega)$ of the low-reflectivity mirror, we obtain a visibility function proportional to $e^{-2\Omega_S^2(T_0 - T/2)^2}$ and axial resolution of $2/\Omega_S$, which is identical to the resolution afforded by Q-OCT. In addition, the $H^*(\Omega)H(-\Omega)$ dependence of PC-OCT will result in even-order dispersion cancellation. Thus, PC-OCT realizes both of these advantages of Q-OCT with an entirely classical experiment.

It is also worth noting that PC-OCT can be (or may even preferably be) operated in

a high-flux regime while Q-OCT cannot, since Q-OCT requires quantum interference and coincidence counting in order to perform a measurement. PC-OCT relies solely on classical interferometry, and thus is operable under a much wider range of conditions, including broad daylight, and data acquisition can be performed extremely rapidly with classical detectors without large dwell times at each axial position.

1.2 Generating phase-sensitive light with parametric downconversion

Spontaneous parametric downconversion (SPDC) was first observed in the 1960's and its properties extensively studied since then [18, 14, 19, 2, 7, 6, 23]. Recently, SPDC has been of particular interest to quantum optics experiments, particularly to generate heralded single photons [10, 21] and entangled photon sources [16, 25]. However, while SPDC is useful in the weakly-pumped regime for quantum optics, few works have exploited the strongly-pumped regime for its strong classical phase-sensitive coherence between the signal and idler beams, which we make use of to implement PC-OCT.

1.2.1 Single-mode parametric fluorescence

We would like to couple our SPDC outputs into a single-mode fibers to ensure maximal phase-sensitive cross-correlations between the signal and idler outputs, as well as for the experimental convenience afforded by fiber optics. As SPDC output is typically highly multimodal, a number of recent studies [17, 16, 4, 3, 11] have explored the idea of manipulating the focusing of the pump beam to concentrate the majority of SPDC output into a single spatial mode. Boyd and Kleinman [5] found that for three-wave mixing interactions with well-defined input spatial modes, the SPDC output power is maximized if $\zeta = L/b = 2.84$, where L is the crystal length, $b = 2n\pi w_0^2/\lambda$ is the confocal parameter in the crystal, w_0 is the beam waist, and n is the crystal's index of refraction at vacuum wavelength λ . Note that the confocal parameter is identical for all three fields (pump, signal, idler).

There are three main factors which affect the spatial mode distribution of the SPDC output [13]: (1) the natural divergence of the SPDC fields due to plane wave pumping over a finite crystal length, (2) angular divergence due to the focusing of the pump beam, and (3) the spectral bandwidth of the signal and idler measurement.

The first contribution can be derived from the longitudinal phase matching condition,

$$\Delta k_z(\theta_{s,i}) = k_p - k_s \cos \theta_s - k_i \cos \theta_i - \frac{2\pi}{\Lambda} = k_s \theta_s^2 \quad (1.12)$$

The phase-matching bandwidth is given by

$$\Delta k_z L = \pi \quad (1.13)$$

where L is the length of the crystal. We then obtain the natural divergence of the signal and idler fields:

$$\theta_{s,j}^- = \sqrt{\frac{\lambda_s}{2n_s L}} \quad (1.14)$$

The second contribution is simply the divergence angle of the pump beam, i.e.

$$\theta_p = \frac{\lambda_p}{\pi n_p w_p} \quad (1.15)$$

where λ_p is the vacuum wavelength of the pump, n_p is the index of the crystal at the pump wavelength, and w_p is the beam waist of the pump at the focus.

The third contribution, which originates from the measurement spectral bandwidth of the signal and idler beams. is negligible if the measurement bandwidth is small compared to the phase-matching bandwidth, as will be the case in this experiment.

For single-mode generation of fluorescence, we try to equate the divergence angle due to pump focusing and the natural divergence angle ($\theta_p = \bar{\theta}_s$), i.e. the spot size of the pump at the waist is only large enough to support a single spatial mode of the degenerate signal and idler beams. This results in a pump focusing parameter of $\xi_p = \pi/2$. The total output divergence from both contributions is then given by $\theta = \sqrt{\bar{\theta}_s^2 + \theta_p^2} = \sqrt{2}\theta_p$. This

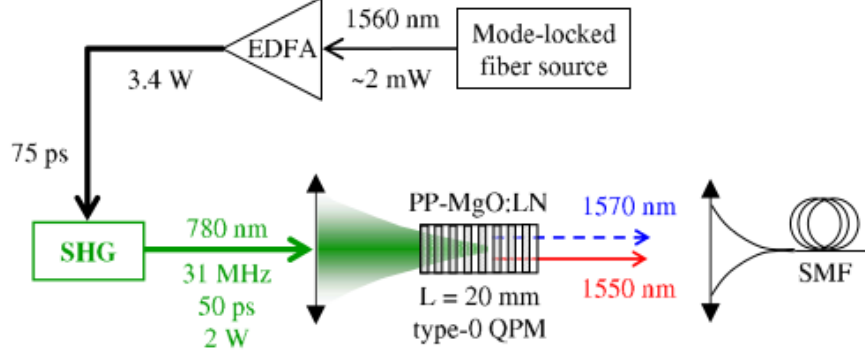


Figure 1-4: Schematic of setup for parametric fluorescence generation and collection in single-mode fiber. We use type 0 phase matching (signal, idler, pump are polarized on the same axis) in a MgO:PPLN crystal.

corresponds to a target focusing parameter of $\xi = \xi_p$ which is larger than the range suggested in Ljunggren and Tengner [17] but close enough to be a starting point for our experiment ($0.5 < \xi_p < 1.5$). Although their calculations indicate that the output ξ_t is 1.5 to 2 times larger than ξ_p , our argument and experimental optimization is closer to $\xi_p = \xi_t$, which is the same conclusion as Boyd and Kleinman [5]. We believe that the measurement bandwidth used in [17] may account for the discrepancy, as our measurement bandwidth is much smaller than the phase-matching bandwidth and thus does not influence the spatial modality of the emission.

Figure 1-4 shows a schematic of the SPDC generation setup. A home-built passively mode-locked pulsed Er-doped fiber laser built with polarization-maintaining fiber [24] was used as a seed source. The center wavelength of 1560 nm was set by a Bragg grating within the laser cavity. The laser generated 75-ps pulses at a repetition rate of ~ 31.1 MHz and

average output power of ~ 1.9 mW, with an output spectrum shown in figure 1-5. This seed laser output was fed into an IPG Photonics Er-doped fiber amplifier (EDFA) with a maximum output of 6 W. In practice, we set the amplifier output power to a lower setting (typically 3-4 W) to avoid the effects of self-phase modulation (SPM), which at high power levels distorts the pulse shape and destroys the transform-limited properties of the pulse. In order to further reduce the effect of SPM, we had the EDFA serviced by IPG Photonics to reduce the internal fiber length to a bare minimum. The spectrum of the output at maximum power setting, before and after modification, is shown in figure 1-6. The EDFA output power showed linear behaviour as a function of drive current, after a minimum threshold of ~ 400 mA, as shown in figure 1-7.

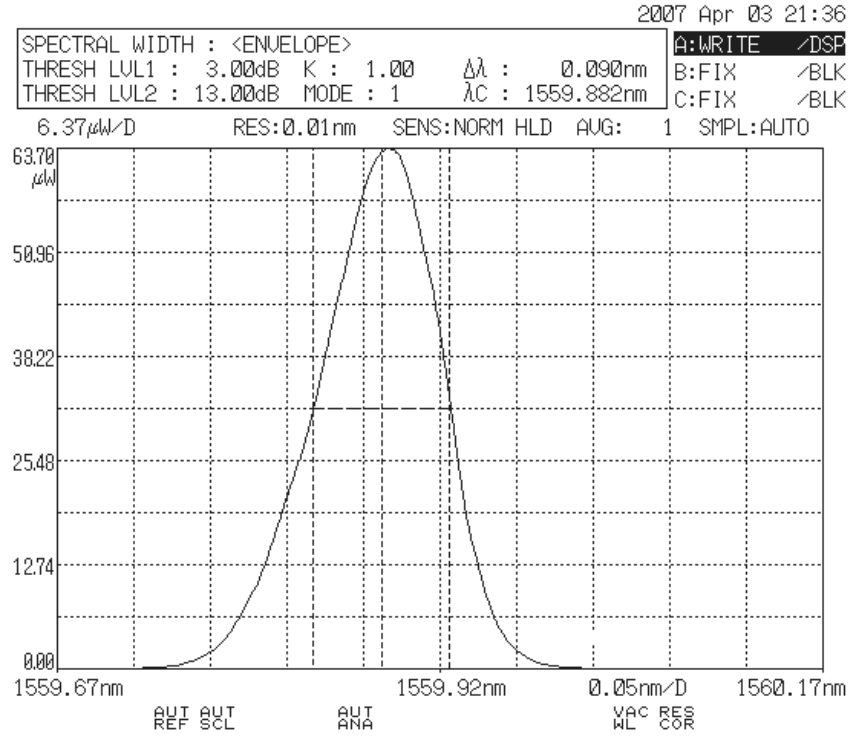
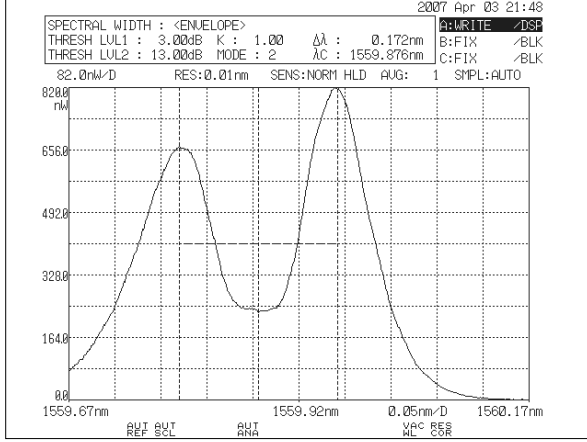
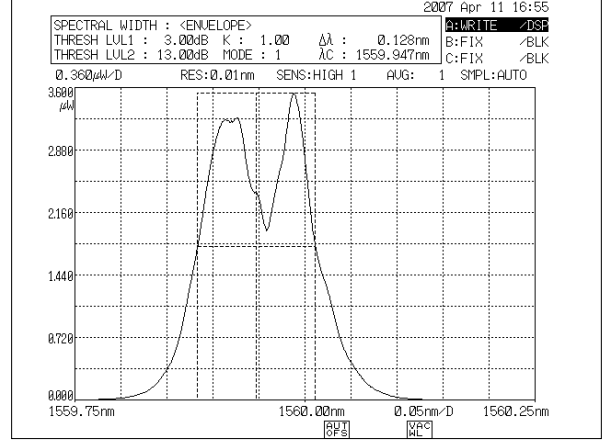


Figure 1-5: Spectrum of a home-built passively mode-locked fiber laser [24] used as a seed source.

We then frequency-doubled the free-space output of the EDFA using a MgO:PPLN crystal with a grating period of $19.47 \mu\text{m}$, inside a temperature-controlled oven at 86.5°C , which was



Before modifications



After modifications

Figure 1-6: EDFA output spectrum at maximum output power setting, before and after modifications by IPG Photonics to remove excess internal fiber. The broadening of the spectrum and double peak is caused by self-phase modulation inside the fiber at high power levels.

phase-matched to produce 50-ps pulses at 780 nm by second harmonic generation (SHG). By focusing the input into the crystal to a waist of 40 μm and careful optimization of the temperature we were able to convert 3.4 W of 1560 nm input into 2 W of output at 780 nm, a conversion efficiency of 59%. The SHG output power is quadratic in the input power in the low efficiency regime, but linear in the high efficiency regime, as shown in figure 1-8. Multiple dichroic mirrors were used to filter out the remaining 1560 nm light. Since we intend to use the 780 nm light to pump an SPDC source at 1560 nm with a second nonlinear crystal, it is important that the strong leftover 1560 nm light from the EDFA is almost completely filtered out with a sufficient number of dichroic mirrors after the SHG stage; we placed enough dichroic mirrors to attenuate the residual 1560 nm power to under 1 nW.

We then optimized the pump focusing for the SPDC using our above theoretic estimate as a starting point by focusing the pump to a waist of 35 μm , which gives $\xi_p = \xi_t \sim 1$. With this focusing fixed, we optimize the coupling of the SPDC output into a single mode SMF-28 fiber, measuring the power at the other end of the fiber using a fiber-coupled InGaAs detector with 10-fW sensitivity. In order to measure the coupling efficiency, we also obtained

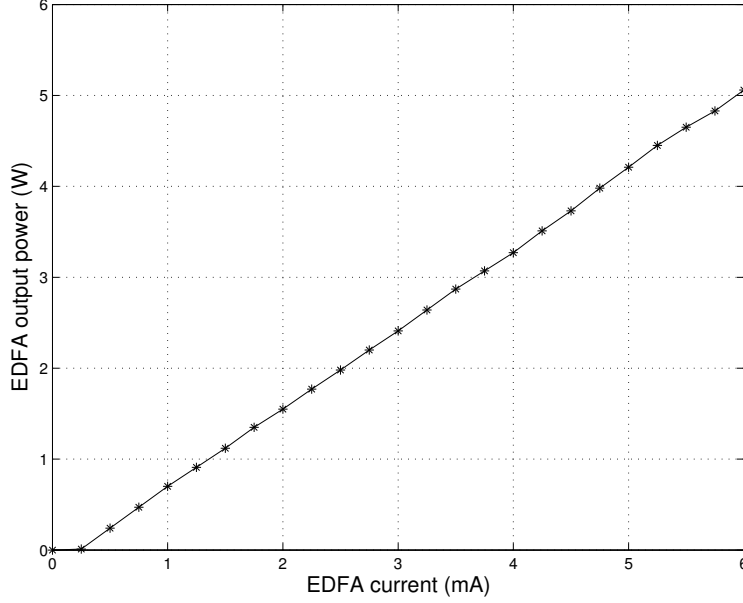


Figure 1-7: EDFA output power (1560 nm) as a function of drive current, showing linear behavior with a threshold of ~ 400 mA.

the total SPDC output power by using a multi-mode fiber in its place. Using this initial setting, we obtained a ratio of $\eta_T = 50\%$. However, to account for the coupling losses and deduce the actual single-mode content of the SPDC output, we connected a single-mode 1550 nm fiber laser source to both our single- and multi-mode fiber inputs and obtained an efficiency of $\eta_f = 82 \pm 2\%$. Our SPDC single-mode content can then be deduced to be $\eta_{SM} = \eta_T / \eta_f = 61 \pm 1.5\%$.

We then varied the pump focusing and repeated the efficiency measurement at each setting. At a waist of $w_p = 25 \mu\text{m}$ we obtained $\eta_T = 57.5\%$ and $\eta_{SM} = 70 \pm 2\%$ which corresponds to $\xi_p = \xi_t = 1.7$. After one crystal shattered under tight focusing, we avoided attempting to focus the pump too tightly to avoid damaging its replacement. Although Fedrizzi et al. found that the optimal focusing parameter lies around the range $0.9 < \xi_p < 1.3$ and $\xi_t < 1.6$ which is slightly different from our result, we attribute this to our much smaller measurement bandwidth in comparison to our phase-matching bandwidth.

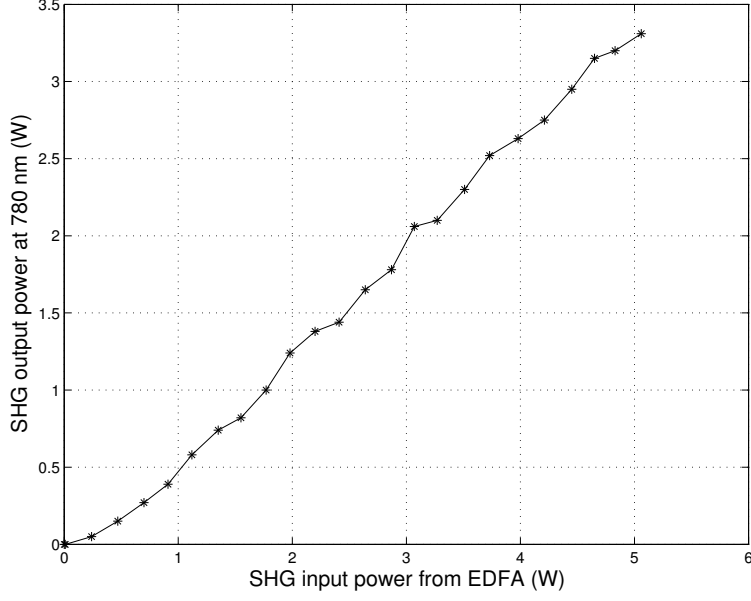


Figure 1-8: SHG output power (780 nm) as a function of input power (1560 nm), showing quadratic dependence at low power levels and linear dependence at high power levels.

1.2.2 SPDC under strong pumping

SPDC is traditionally used in the low-flux regime to generate biphoton and entangled photon states. However, in this experiment we are interested not in the quantum properties of SPDC but merely the phase-sensitive cross-correlations between the signal and idler. Thus, it is useful to have strong pumping beyond this low-flux regime. While in the low-flux regime, the SPDC power output is linear in the pump power, as the pump power is increased sufficiently, the SPDC output enters a regime of exponential dependence, due to the parametric amplification of the parametric fluorescence itself before exiting the crystal. This parametric amplification incidentally also breaks any entanglement properties of the SPDC outputs, but PC-OCT does not make use of quantum entanglement; in the amplified regime, the signal and reference beams will continue to have classically-maximal phase-sensitive coherence which is sufficient for the experiment. Figure 1-9 shows that for our setup, we enter this regime at pump powers greater than 0.5 W - 1 W. It is also worth noting that as we enter this regime, the SPDC output bandwidth gains a linear dependence on pump power, shown

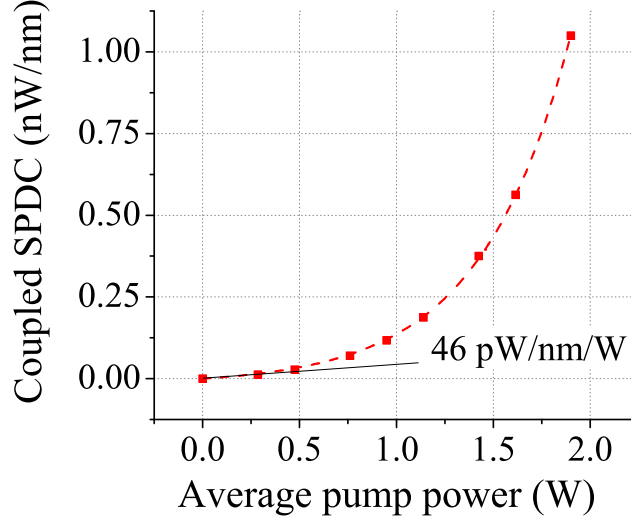


Figure 1-9: SPDC output power as a function of pump power, showing the linear dependence in the low-flux regime and exponential dependence in the high-flux (amplified) regime.

in figure 1-10(b).

1.3 Experimental setup

We now turn to using our SPDC-based phase-sensitive light source to set up and demonstrate PC-OCT. In this section, we devise a method to interrogate the same sample twice with phase conjugation, a simulation of sample dispersion using a long fiber spool to demonstrate dispersion cancellation, a classical interferometric measurement, and an automated positioning and data collection system.

1.3.1 SPDC source

We couple the SPDC light previously described into the input of a 4-channel JDS Uniphase course wavelength division multiplexer (CWDM) with center wavelengths at 1530 nm, 1550 nm, 1570 nm, and 1590 nm, with nearly flat-top passbands of 18 nm width at each channel, as shown in figure 1-12. We use the 1550 nm channel as the reference and the 1570 nm

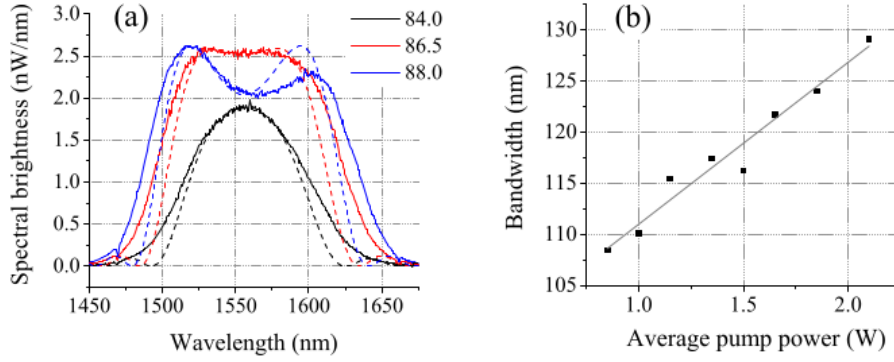


Figure 1-10: (a) Power spectral densities (solid) and theoretical models based on Sellmeier coefficients (dashed) for various crystal temperatures, with pump power fixed at 2 W. (b) Linear dependence of SPDC output bandwidth as a function of pump power, with temperature fixed at 86°C.

channel as the signal.

1.3.2 Double-pass configuration and phase conjugation

PC-OCT requires that the signal light passes through the same target twice before an interference measurement with the idler beam. We accomplish this double-pass configuration using a polarizing beamsplitter (PBS) and quarter-waveplate as shown in figure 1-11.

We do this by first sending the light in second, identical CWDM but configured in reverse (i.e. we injecting the light into the 1570 nm channel and collect the light at the common port). We then collimate the output and configure it to be horizontally polarized using polarization control paddles. The horizontally polarized light then passes through a polarizing beamsplitter (PBS) unreflected, followed by a quarter-waveplate, which leaves it in a circular polarization before interacting with the target. The reflected light passes through the same waveplate on the return path, converting it to a vertical polarization, which upon returning to the PBS is reflected into an optical parametric amplifier (OPA) which performs the phase conjugation using a third MgO:PPLN crystal of the same poling period. Parametric amplification necessitates that the pulsed pump light and the pulsed

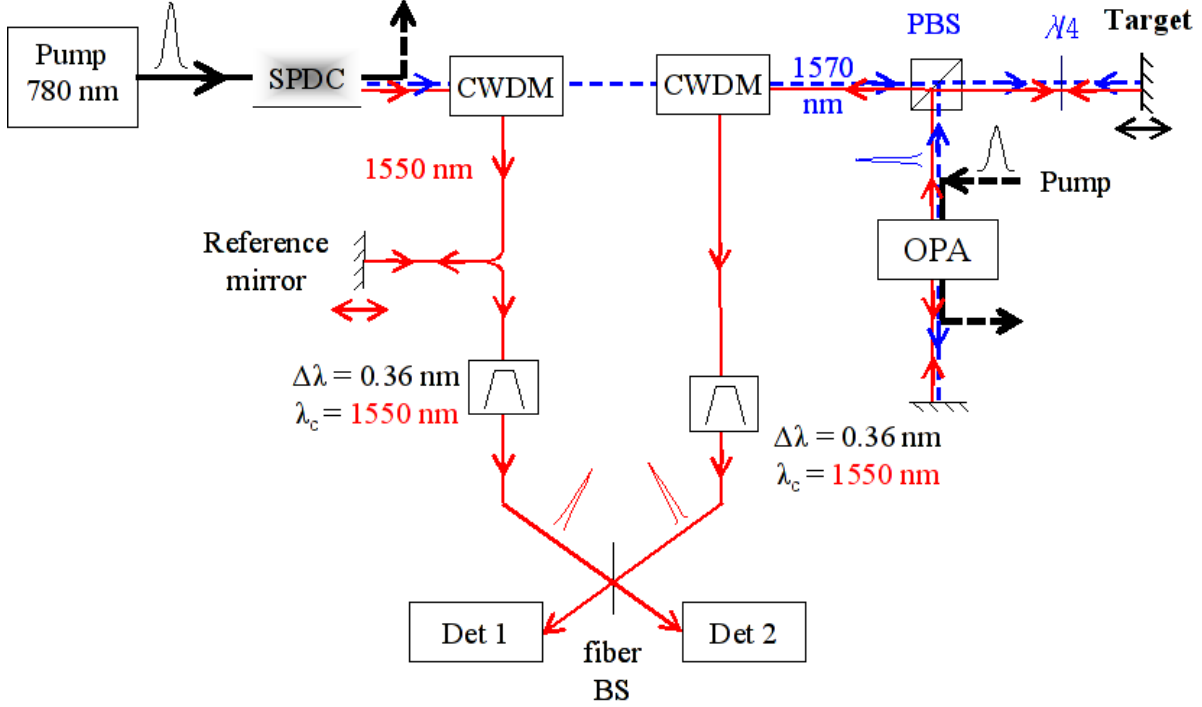


Figure 1-11: PC-OCT experimental setup. CWDM: Course Wavelength Division Multiplexer, OPA: Optical Parametric Amplifier, PBS: Polarizing Beamsplitter.

return signal are matched in time, which we accomplish by re-using the leftover 780 nm pulsed pump signal from the second (SPDC) crystal with a free-space variable delay. In this experiment, the 50 ps pump pulse limits the range of targets to a maximum axial displacement of ~ 15 mm, beyond which parametric amplification will not occur, although it is in principle possible to translate the pump and target simultaneously to accomodate larger ranges.

The reflected, phase-conjugated light then follows the entire optical path in reverse and is re-coupled back into the second CWDM. Since we pump the OPA at 780 nm, the phase-conjugated beam is now at 1550 nm and exits the CWDM from its 1550 nm port, and is ready for interference measurement with the 1550 nm reference arm.

We additionally install fiber-coupled filters on both reference and signal (after conjugation) arms. The filters have Lorentzian spectral profiles with widths of $\Delta\lambda = 0.36$ nm and tunable center wavelengths near 1550 nm, and transmission of $\sim 45\%$, setting the measure-

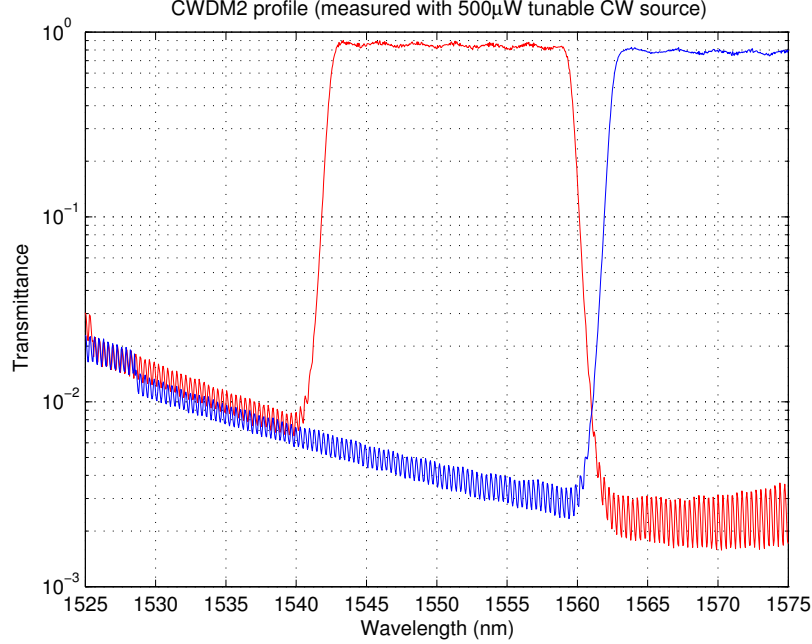


Figure 1-12: Transmittance of 1550 nm and 1570 nm channels of the CWDM, scanned using a InGaAs detector and tunable fiber-coupled laser with a maximum wavelength of 1575 nm, showing nearly flat-top transmission and sharp falloff, allowing the reference and signal to be efficiently separated.

ment bandwidth narrow enough for signal and idler beams to be in corresponding single spatial modes.

1.3.3 Dispersion simulation using long fiber spool

At the pulse width of 50 ps we use in our experiment, typical free-space optics cannot easily provide sufficient dispersion to test the even-order dispersion-cancelling properties of PC-OCT; however, sample dispersion becomes a significant issue for OCT experiments involving thick samples and femtosecond lasers. For testing purposes, we simulate sample dispersion by inserting ~ 50 meters of SMF-28 fiber (with a dispersion of 17 ps/nm/km) in the signal arm. In the reference arm, we do not wish to deliberately induce dispersion, but it is necessary to match the optical path length of the signal arm in order to perform an interferometric measurement. Since zero dispersion fiber is not widely available, we used

Corning LEAF fiber, a widely-available nonzero dispersion-shifted fiber commonly used for telecommunications with a dispersion of ~ 4 ps/nm/km at 1560 nm. Although this dispersion will not be cancelled by PC-OCT, it is much lower than the SMF-28 fiber used in the signal arm. The reference arm needed a total of 135 m of LEAF fiber to match the total optical length of SMF-28 in signal arm. This length was measured by injecting pulses into both arms performing time-of-flight measurement using high-speed InGaAs photodetectors.

We observed that the index of refraction of fiber was significantly affected by changes in the ambient temperature; the fluctuations in room temperature by ± 1 degree were enough to cause several millimetres of difference in effective optical length after the ~ 135 m of fiber length used in the experiment. We confirmed this by monitoring the changes in room temperature, as shown in graph 1-13, and alleviated the problem by placing the bulk of the fiber spool inside a thermally-insulating foam container, performing successive measurements within a short time frame, and monitoring the room temperature carefully to ensure consistent measurement conditions.

1.3.4 Interferometric measurement

Interferometric measurement was performed by combining both signal and reference arms using a 50/50 fiber beam splitter. A fiber circulator and free-space delay facilitate the ability to fine-tune the optical path length difference of the two arms. A constantly vibrating piezoelectric actuator was added to the free-space delay in order to continuously scan the interferometer over a full wavelength at each position and measure the interference visibility.

1.3.5 Data collection

We connected both interferometer outputs to two channels of a high-sensitivity (0.1 pW) HP8163A InGaAs power meter, and linked to a computer via GPIB connection. A custom Visual Basic program was written to synchronously drive the PicoMotor stages and read values from both channels of the power meter. The PZT mirror was set to vibrate at a frequency of 80 Hz, intentionally slower than the averaging time of the power meter,

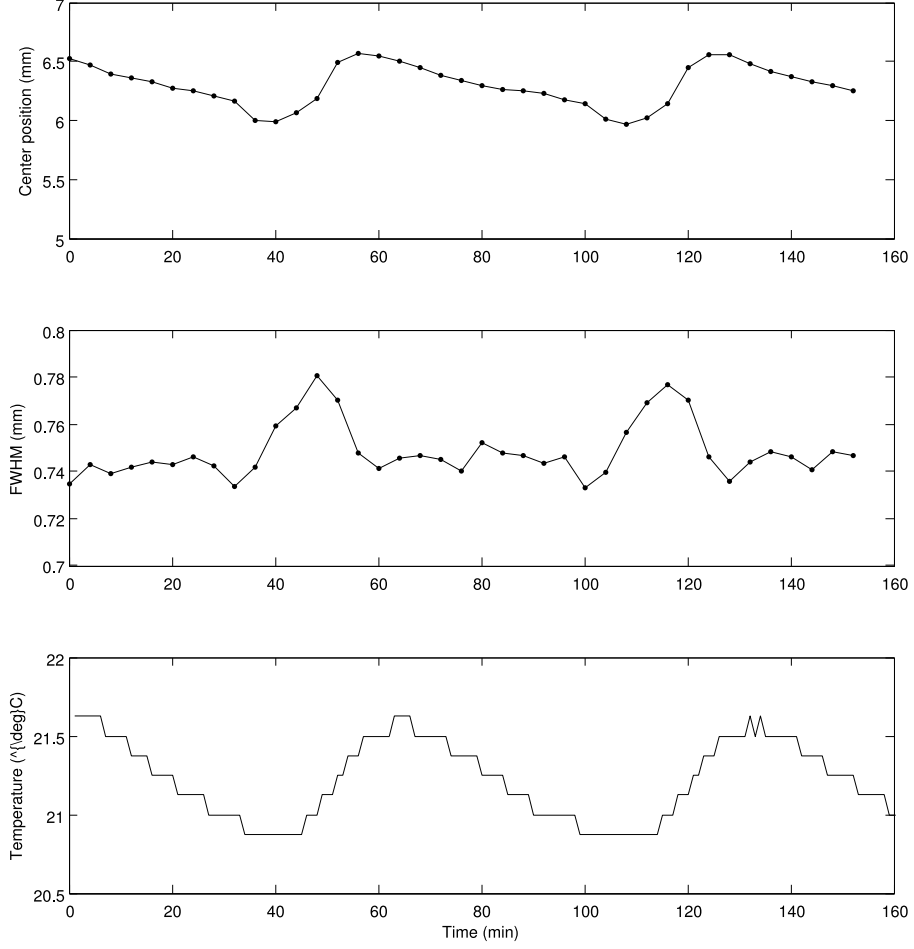


Figure 1-13: (a) Center position and (b) FWHM of the PC-OCT interferometric envelope, with (c) synchronized measurements of the ambient room temperature, showing the effect of temperature on the index of refraction of the long fibers in the experiment.

allowing the program to read the interference amplitude by logging a series of power values from the power meter with the stage stationed at any point. The interference amplitude was normalized to the sum of power outputs from both channels in order to compensate for laser power fluctuations.

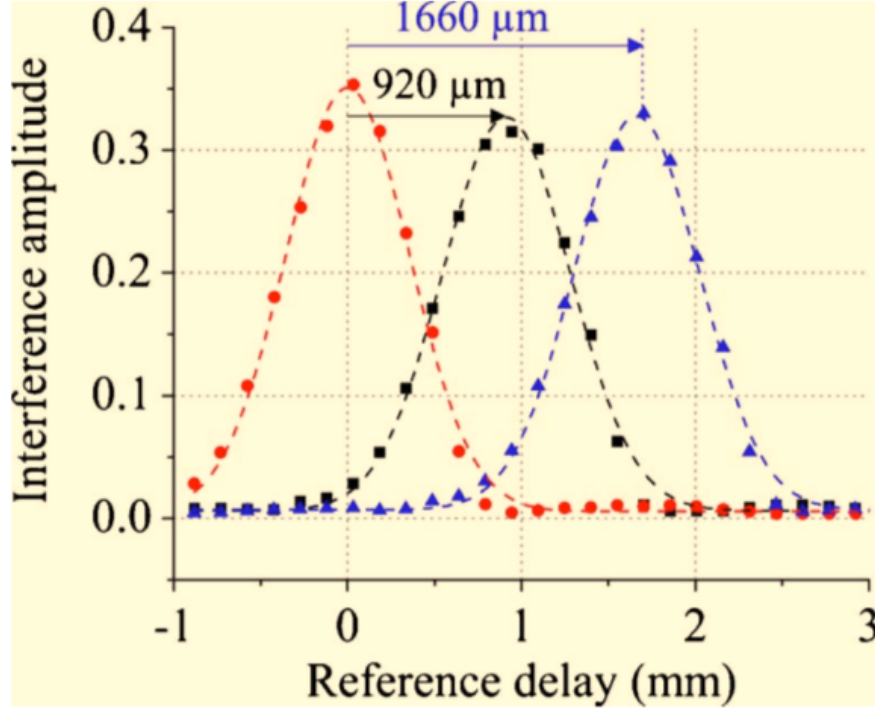


Figure 1-14:

1.4 Results

Using a high reflectivity mirror as a target, figure 1-14 shows the results of three successive scans of the target with a relative separation of $\Delta z = 450 \mu\text{m}$. Given the double-pass configuration, one would expect the resulting peaks to have a relative separation of $\Delta z_R = 2\Delta z$ giving us a $2\times$ axial improvement. The observed shifts were $920 \pm 20 \mu\text{m}$ and $1660 \pm 20 \mu\text{m}$, confirming this behavior; the discrepancy in the right peak from the expected $\sim 1800 \mu\text{m}$ is likely attributable to room temperature fluctuation as described earlier. Note that this effect is particularly noticable because we deliberately added long fibers to induce dispersion.

Besides the $2 \times$ axial resolution improvement, we expect to observe cancellation of even-order dispersion in the signal arm. The expected width of the interference envelope is given

by the convolution of the signal and reference fields, accounting for dispersion:

$$L_{OCT}^2 = 4L_0^2 + (c\Delta\lambda_F)^2(D_S(z_{S1} - z_{S2}) + D_R z_R) \quad (1.16)$$

where $z_{S1} = 77.1$ metres is the length of fiber in the signal arm before conjugation, $z_{S2} = 71.2$ is the length of fiber after conjugation (leaving a net 5.9 meters of fiber in which dispersion is not cancelled in the signal arm), $z_R = 135$ meters is the length of fiber in the reference arm, and D_S and D_R are the dispersion coefficients in the signal and reference arms, respectively. Since we intend to deliberately induce dispersion in the signal arm to demonstrate the dispersion-cancelling properties of PC-OCT, we use standard SMF-28 fiber which has $D_S = 17$ ps/nm/km. The length of fiber in the reference arm was chosen to match the signal arm for interferometric measurement; we do not intend to deliberately induce dispersion in the reference arm, in order to demonstrate the dispersion-cancelling properties of the phase-conjugating signal arm. However, as zero-dispersion fiber was not available, we used LEAF fiber, a commonly-used nonzero dispersion shifted fiber (NZ-DSF) designed for telecommunications and with a dispersion of $D_R = 4.2$ ps/nm/km. Using these values, we obtain a predicted FWHM of $L_{OCT} = 893 \pm 30 \mu\text{m}$ which is in excellent agreement with the measured width of $890 \pm 30 \mu\text{m}$. If dispersion had not been cancelled, we would flip the sign of z_{S2} :

$$L_{OCT}^2 = 4L_0^2 + (c\Delta\lambda_F)^2(D_S(z_{S1} + z_{S2}) + D_R z_R) \quad (1.17)$$

This yields $L_{OCT} = 3.02$ mm, over three times our measured value, suggesting that dispersion cancellation was achieved almost perfectly in the signal arm.

We see that PC-OCT recovers both of the main advantages previously associated with Q-OCT using an entirely classical setup. In addition, Erkmen showed [8] that as long as the conjugator gain $|V|^2$ is large and reflected field strong, the signal-to-noise ratio (SNR) of PC-OCT is similar to that of C-OCT, which is expected since they employ a similar principle of operation. On the other hand, Q-OCT relies on SPDC to generate entangled photon states and thus necessitates operation at extremely low flux and Geiger-mode avalanche

photodetection to observe fourth-order Hong-Ou-Mandel interference, which significantly limits acquisition speed and operating conditions.

PC-OCT owes its resolution advantage to its double-pass configuration. However, an intimate relationship between this and Q-OCT can be seen in Abouraddy’s interpretation of Q-OCT [1] which accounts for the $H^*(\Omega)H(-\Omega)$ term as a product of an actual sample illumination and a virtual sample illumination, which in PC-OCT is manifested in two successive illuminations. PC-OCT’s double-pass configuration providing an axial advantage over C-OCT also leads us to consider the possibility of C-OCT in a double-pass configuration, with phase-insensitive sources and no phase conjugation. Although a resolution advantage would be obtained, even-order dispersion would be doubled instead of cancelled [9].

1.5 Conclusions

Recent developments in quantum optics have led to new methods in sensing that involve entangled biphotons and other nonclassical states of light to achieve advantages over their conventional counterparts. In particular, Q-OCT uses quantum interferometry to achieve a two-fold resolution improvement and even-order dispersion cancellation over C-OCT. Although these advantages have been proposed and demonstrated, we begin to question the true nature of the claimed advantages of these quantum techniques, whether those advantages are truly quantum in nature, and moreover, if there is an unconventional classical method to achieve the same.

In particular, we demonstrate experimentally through PC-OCT that Q-OCT’s advantages, although realizable using quantum interferometry, arise from the phase-sensitive cross-correlations in the signal and idler beams and are realizable using a novel classical technique. In addition, PC-OCT is operable at much higher light levels and acquisitions may be performed extremely rapidly, incorporating the best advantages of classical sensing.

In this work, we also address the experimental implementation issue of PC-OCT. Most classical light sources have only phase-insensitive cross-correlations and zero phase-sensitive cross-correlations. Our setup requires strong and broadband phase-sensitive cross-correlations

between signal and idler beams, which in principle can be produced by splitting a laser beam and imposing anti-correlated phase noises on both beams using modulators. However, in this work, we demonstrate an approach that employs nonlinear optics. We consider the SPDC sources used to generate biphoton states with phase-sensitive cross-correlations for quantum optics experiments, but operated in a strong-pump, high-flux regime in which photons are amplified before exiting the crystal. Although this destroys their entanglement properties, the phase-sensitive cross-correlations are preserved perfectly which is sufficient to implement PC-OCT, which makes no use of quantum interference. We implemented such a source and carried out a PC-OCT experiment, demonstrating the realizability of strong, phase-sensitive classical light sources which, while unconventional, are not beyond the limits of classical physics, and may be useful for a variety of other sensing applications.

Bibliography

- [1] Ayman F. Abouraddy, Magued B. Nasr, Bahaa E. A. Saleh, Alexander V. Sergienko, and Malvin C. Teich. Quantum-optical coherence tomography with dispersion cancellation. *Phys. Rev. A*, 65:053817, May 2002.
- [2] S. A. Akhmanov, O. N. Chunaev, V. V. Fadeev, R. V. Khokhlov, D. N. Klyshko, A. I. Kovrigin, and A. S. Piskarskas. Parametric Generators of Light. In J. Fox, editor, *Modern Optics*, page 343, 1967.
- [3] Ryan S. Bennink, Yun Liu, D. Duncan Earl, and Warren P. Grice. Spatial distinguishability of photons produced by spontaneous parametric down-conversion with a focused pump. *Phys. Rev. A*, 74:023802, Aug 2006.
- [4] Fabio Antonio Bovino, Pietro Varisco, Anna Maria Colla, and Er V. Sergienko. Effective fiber-coupling of entangled photons for quantum communication, opt. *Commun*, pages 343–348, 2003.
- [5] G. D. Boyd and D. A. Kleinman. Parametric Interaction of Focused Gaussian Light Beams. *Journal of Applied Physics*, 39:3597–3639, July 1968.
- [6] David C. Burnham and Donald L. Weinberg. Observation of simultaneity in parametric production of optical photon pairs. *Phys. Rev. Lett.*, 25:84–87, Jul 1970.
- [7] R. L. Byer and S. E. Harris. Power and bandwidth of spontaneous parametric emission. *Phys. Rev.*, 168:1064–1068, Apr 1968.

- [8] Baris I. Erkmen. *Phase-Sensitive Light: Coherence Theory and Applications to Optical Imaging*. PhD thesis, Massachusetts Institute of Technology, May 2008.
- [9] Baris I. Erkmen and Jeffrey H. Shapiro. Phase-conjugate optical coherence tomography. *Phys. Rev. A*, 74:041601, Oct 2006.
- [10] Sylvain Fasel, Olivier Alibart, Sbastien Tanzilli, Pascal Baldi, Alexios Beveratos, Nicolas Gisin, and Hugo Zbinden. High-quality asynchronous heralded single-photon source at telecom wavelength. *New Journal of Physics*, 6(1):163, 2004.
- [11] Alessandro Fedrizzi, Thomas Herbst, Andreas Poppe, Thomas Jennewein, and Anton Zeilinger. A wavelength-tunable fiber-coupled source of narrowband entangled photons. *Opt. Express*, 15(23):15377–15386, Nov 2007.
- [12] J. D. Franson. Nonlocal cancellation of dispersion. *Phys. Rev. A*, 45:3126–3132, Mar 1992.
- [13] Julien Le Gouët, Dheera Venkatraman, Franco N. C. Wong, and Jeffrey H. Shapiro. Classical low-coherence interferometry based on broadband parametric fluorescence and amplification. *Opt. Express*, 17(20):17874–17887, Sep 2009.
- [14] S. E. Harris, M. K. Oshman, and R. L. Byer. Observation of tunable optical parametric fluorescence. *Phys. Rev. Lett.*, 18:732–734, May 1967.
- [15] C. K. Hong, Z. Y. Ou, and L. Mandel. Measurement of subpicosecond time intervals between two photons by interference. *Phys. Rev. Lett.*, 59:2044–2046, Nov 1987.
- [16] Christian Kurtsiefer, Markus Oberparleiter, and Harald Weinfurter. High-efficiency entangled photon pair collection in type-ii parametric fluorescence. *Phys. Rev. A*, 64:023802, Jul 2001.
- [17] Daniel Ljunggren and Maria Tengner. Optimal focusing for maximal collection of entangled narrow-band photon pairs into single-mode fibers. *Phys. Rev. A*, 72:062301, Dec 2005.

- [18] W. H. Louisell, A. Yariv, and A. E. Siegman. Quantum fluctuations and noise in parametric processes. i. *Phys. Rev.*, 124:1646–1654, Dec 1961.
- [19] Douglas Magde and Herbert Mahr. Study in ammonium dihydrogen phosphate of spontaneous parametric interaction tunable from 4400 to 16 000 Å. *Phys. Rev. Lett.*, 18:905–907, May 1967.
- [20] Magued B. Nasr, Bahaa E. A. Saleh, Alexander V. Sergienko, and Malvin C. Teich. Demonstration of dispersion-canceled quantum-optical coherence tomography. *Phys. Rev. Lett.*, 91:083601, Aug 2003.
- [21] T.B. Pittman, B.C. Jacobs, and J.D. Franson. Heralding single photons from pulsed parametric down-conversion. *Optics Communications*, 246(46):545 – 550, 2005.
- [22] A. M. Steinberg, P. G. Kwiat, and R. Y. Chiao. Dispersion cancellation in a measurement of the single-photon propagation velocity in glass. *Phys. Rev. Lett.*, 68:2421–2424, Apr 1992.
- [23] P. R. Tapster, J. G. Rarity, and J. S. Satchell. Use of parametric down-conversion to generate sub-poissonian light. *Phys. Rev. A*, 37:2963–2967, Apr 1988.
- [24] Dheera Venkatraman. Tools for quantum optics : pulsed polarization-maintaining er-doped fiber laser and spatial mode manipulation in spontaneous parametric downconversion. Master’s thesis, Massachusetts Institute of Technology, 2007.
- [25] F.N.C. Wong, J.H. Shapiro, and T. Kim. Efficient generation of polarization-entangled photons in a nonlinear crystal. *Laser Physics*, 16(11):1517–1524, 2006.